Progress In Electromagnetics Research, PIER 88, 197–211, 2008

FDTD INVESTIGATION ON BISTATIC SCATTERING FROM A TARGET ABOVE TWO-LAYERED ROUGH SURFACES USING UPML ABSORBING CONDITION

J. Li, L.-X. Guo, and H. Zeng

School of Science
Xidian University
No. 2, Taibai Road, Xi'an, Shaanxi, China

Abstract—This paper presents an investigation for the electromagnetic scattering characteristic of the 2-D infinitely long target located above two-layered 1-D rough surfaces. A finite-difference time-domain (FDTD) approach is used in this study, and the uniaxial perfectly matched layer (UPML) medium is adopted for truncation of FDTD lattices, in which the finite-difference equations can be used for the total computation domain by properly choosing the uniaxial parameters. The upper and lower interfaces are characterized with Gaussian statistics for the height and the autocorrelation function. For the composite scattering of infinitely long cylinder and underlying single-layered rough surfaces as an example, the angular distribution of scattering coefficient with different incident angles is calculated and it shows good agreement with the numerical result by the conventional method of moments. And the influence of some parameters related to the two-layered rough surfaces and target on composite scattering coefficient is investigated and discussed in detail.

1. INTRODUCTION

In recent years, the composite electromagnetic scattering between the randomly rough surface and target has attached considerable interest in the fields of radar surveillance, target tracking, oceanic remote sensing, etc. However, the study of such electromagnetic scattering model is a complex and difficult subject due to the complicated interactions from the target and underlying rough surface. Some methods have been to deal with the problem, taking for example, the "four-path" method [1], the image technique [2], the high-frequency method [3], and the calculation technique based on physical optics

approximation [4] have been investigated for a target above a flat surface. The hybrid SPM/MOM technique [5] and the method of moments [6] are employed to calculate the scattering of target above on a rough surface. The finite-element method with domain decomposition and generalized forward-backward method [7, 8] were analyzed for the electromagnetic scattering from target located above an ocean-like rough surface. We have also studied the light scattering from a spherical particle above a slightly rough surface [9] and the electromagnetic scattering from a target above the rough sea surface [10].

In all references mentioned above, the rough surface is assumed to be a single homogeneous layer. The scattering of two-layered rough surfaces without object are investigated in [11, 12]. Ei-shenawee M. studied the polarimetric scattering from two-layered random rough surfaces with and without buried objects [13], and Chew et al. [14] focus on their research on the scattering characteristic from objects above the multilayered medium with flat interfaces. However, only few researchers analyzed the electromagnetic scattering from the target placed above multilayered rough surfaces. In this paper, the finite-difference time-domain (FDTD) algorithm with UPML absorbing boundary is utilized to analyze the electromagnetic scattering from the 2-D infinitely long target above two-layered 1-D randomly rough surfaces. The uniaxial perfectly matched layer medium is placed at the outer extremities of the mesh. In the uniaxial medium the finite-difference equations are suitable for all the computation domain due to the field satisfy Maxwell's equations, which makes the algorithm convenient and accordant. The paper is organized as follows: the theoretical formulae of calculating composite scattering field by FDTD are developed in Section 2. Numerical results of the composite scattering of target and underlying two-layered rough surfaces are presented and discussed in Section 3 for different conditions, which include the dielectric constants of two-layered rough surfaces, the thickness of upper medium layer, as well as the size and dielectric constants of target. Section 4 ends with the conclusions of the paper and proposed the further investigation in this topic.

2. SCATTERING FROM TARGET AND TWO-LAYERED ROUGH SURFACES

The geometry for 2-D infinitely long target and underlying two-layered rough surfaces is shown in Fig. 1, where the composite model is composed of three homogeneous layers: the air, the upper medium layer with the finite thickness H, and the lower medium layer with

infinite depth. The upper and lower interfaces are characterized with Gaussian statistics for the height and the autocorrelation function. And the target is located at the altitude h from its center to the mean location of upper rough surface. Let ε_1, ε_2, ε_3, ε_4 represent the relative dielectric constants of the air, the target, the upper medium layer and the lower medium layer, respectively.

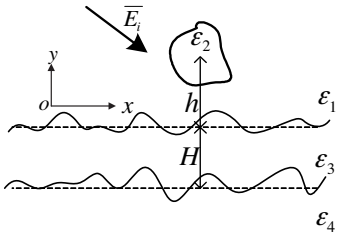

Figure 1. Geometry for target above two-layered rough surfaces.

2.1. Simulation of Rough Surface and FDTD Model

In this section, the rough interface with Gaussian spectrum in Fig. 1 is simulated by Monte Carlo method. It is assumed that the length of rough surface is L, the number of the point discretized at equal interval is $N+1$, and the distance of two adjacent points is Δx, where $L = N \cdot \Delta x$. The altitude of each point $x_n = n\Delta x (n = 1, \ldots, N)$ on the rough surface is defined as [15]

$$\zeta(x_n) = \frac{1}{L} \sum_{i=-N/2}^{N/2-1} F(k_i) e^{-jk_i x_n} \tag{1}$$

where, for $i \geq 0$

$$F(k_i) = \left[2\pi L W(k_i)\right]^{1/2} \cdot \begin{cases} \left[N(0,1) + jN(0,1)\right]/\sqrt{2} & i \neq 0, N/2 \\ N(0,1) & i = 0, N/2 \end{cases} \tag{2}$$

For $i < 0$, $F(k_i) = F(k_{-i})^*$, where the asterisk implies complex conjugate. $N(0,1)$ is a random variant with a Gaussian distribution of zero mean and unit variance. $k_i = 2\pi i/L$, and $W(k_i)$ is the Gaussian power spectrum function, i.e.,

$$W(k_i) = (l\delta^2/2\sqrt{\pi}) e^{-k_i^2 l^2/4} \tag{3}$$

where δ denotes the rms height and l is the correlation length. And k_i is the spatial frequency in the x direction. Usually Equation (1) is carried out with a Fast Fourier Transform (FFT).

It is important to know the division of the computation region with FDTD algorithm in calculating electromagnetic scattering from a target above two-layered rough surfaces (see Fig. 2). The incident wave is generated on the connective boundary, and the UPML absorbing medium is the outer boundary of FDTD region. In addition, output boundary must be set to do a near-to-far transformation to obtaining the far fields. In what follows, the three boundaries will be investigated at length.

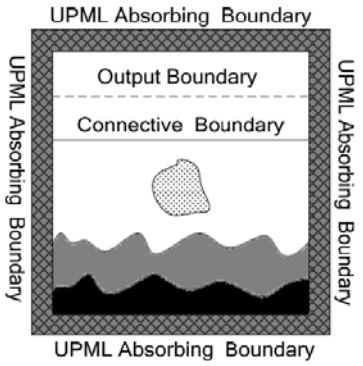

Figure 2. Division model of computation region for the FDTD algorithm.

2.2. UPML Absorbing Boundary

In theory, the computation domain should be unbounded for the scattered field existing in infinite free space. But no computer can store an unlimited amount of date. To deal with the conflict, a virtual absorbing boundary (see Fig. 2) must be built, and the outgoing waves have to propagate outward without non-physical reflection from the boundary. There have been many absorbing boundary conditions developed to implement this in the FDTD method. Where, the UPML absorbing medium [16, 17] are used to terminate the FDTD lattices, in which the finite-difference equations can be used for the total computation domain due to the fields satisfying Maxwell's equations (Ampere's and Faraday's laws). This makes the algorithm efficient since one does not have to take special care of the interface plane between the boundary and the interior regions. In addition, the uniaxial medium can be perfectly matched to an interior lossy medium without any modification except for properly choosing the uniaxial parameters. For the 2-D Maxwell's equations, only E_z-, H_x-, H_y-field components (TM case)/H_z-, E_x-, E_y-field components (TE case) are

nonzero. In the uniaxial medium, the Faraday's laws for TM waves is expressed as

$$\left.\begin{aligned}\frac{\partial E_z}{\partial y} &= -jw\mu_1\frac{s_y}{s_x}H_x \\ \frac{\partial E_z}{\partial x} &= jw\mu_1\frac{s_x}{s_y}H_y\end{aligned}\right\} \tag{4}$$

And the Ampere's laws is

$$\frac{\partial H_y}{\partial x} - \frac{\partial H_x}{\partial y} = (jw\varepsilon_1 + \sigma_1)s_x s_y E_z \tag{5}$$

where, ε_1, μ_1, σ_1 represent the parameters of interior medium. s_x and s_y are only spatially variant along the x and y directions, and $s_x = k_x + \sigma_x/jw\varepsilon_0$, $s_y = k_y + \sigma_y/jw\varepsilon_0$, referring to [16]. In Equation (4), the intermediate variables B_x and B_y are introduced as

$$B_x = \frac{\mu_1}{s_x}H_x \qquad B_y = \frac{\mu_1}{s_y}H_y \tag{6}$$

And in Equation (5), the intermediate variables P'_z and P_z are inserted as

$$P'_z = s_y s_x E_z \qquad P_z = P'_z/s_x \tag{7}$$

Using a Fourier transform where $jw \to \partial/\partial t$, the Faraday's laws can be transformed into the time domain. Thus the magnetic fields are obtained by the following relations $E_z \to B_x$, $B_y \to H_x$, H_y

$$\frac{\partial E_z}{\partial y} = -k_y\frac{\partial B_x}{\partial t} - \frac{\sigma_y}{\varepsilon_0}B_x \tag{8a}$$

$$k_x\frac{\partial B_x}{\partial t} + \frac{\sigma_x}{\varepsilon_0}B_x = \mu_1\frac{\partial H_x}{\partial t} \tag{8b}$$

$$\frac{\partial E_z}{\partial x} = k_x\frac{\partial B_y}{\partial t} + \frac{\sigma_x}{\varepsilon_0}B_y \tag{9a}$$

$$k_y\frac{\partial B_y}{\partial t} + \frac{\sigma_y}{\varepsilon_0}B_y = \mu_1\frac{\partial H_y}{\partial t} \tag{9b}$$

Similarly, for the Ampere's laws the electric field is deduced by the relations H_x, $H_y \to P'_z \to P_z \to E_z$

$$\frac{\partial H_y}{\partial x} - \frac{\partial H_x}{\partial y} = \varepsilon_1\frac{\partial P'_z}{\partial t} + \sigma_1 P'_z \tag{10a}$$

$$\frac{\partial P_z'}{\partial t} = k_x \frac{\partial P_z}{\partial t} + \frac{\sigma_x}{\varepsilon_0} P_z \tag{10b}$$

$$\frac{\partial P_z}{\partial t} = k_y \frac{\partial E_z}{\partial t} + \frac{\sigma_y}{\varepsilon_0} E_z \tag{10c}$$

Using central difference approximation, the difference expressions of Equations (8)–(10) are as follows

$$B_x^{n+\frac{1}{2}}\left(i, j+\frac{1}{2}\right) = \frac{\frac{k_y(m)}{\Delta t} - \frac{\sigma_y(m)}{2\varepsilon_0}}{\frac{k_y(m)}{\Delta t} + \frac{\sigma_y(m)}{2\varepsilon_0}} \cdot B_x^{n-\frac{1}{2}}\left(i, j+\frac{1}{2}\right) - \frac{\frac{1}{\Delta y}}{\frac{k_y(m)}{\Delta t}+\frac{\sigma_y(m)}{2\varepsilon_0}} \cdot \left(E_z^n(i, j+1) - E_z^n(i, j)\right) \tag{11}$$

$$H_x^{n+\frac{1}{2}}\left(i, j+\frac{1}{2}\right) = H_x^{n-\frac{1}{2}}\left(i, j+\frac{1}{2}\right) + \frac{\frac{k_x(m)}{\Delta t} + \frac{\sigma_x(m)}{2\varepsilon_0}}{\mu_1/\Delta t} \cdot B_x^{n+\frac{1}{2}}\left(i, j+\frac{1}{2}\right) - \frac{\frac{k_x(m)}{\Delta t} - \frac{\sigma_x(m)}{2\varepsilon_0}}{\mu_1/\Delta t} \cdot B_x^{n-\frac{1}{2}}\left(i, j+\frac{1}{2}\right) \tag{12}$$

$$B_y^{n+\frac{1}{2}}\left(i+\frac{1}{2}, j\right) = \frac{\frac{k_x(m)}{\Delta t} - \frac{\sigma_x(m)}{2\varepsilon_0}}{\frac{k_x(m)}{\Delta t} + \frac{\sigma_x(m)}{2\varepsilon_0}} \cdot B_y^{n-\frac{1}{2}}\left(i+\frac{1}{2}, j\right) + \frac{\frac{1}{\Delta x}}{\frac{k_x(m)}{\Delta t} + \frac{\sigma_x(m)}{2\varepsilon_0}} \cdot \left(E_z^n(i+1, j) - E_z^n(i, j)\right) \tag{13}$$

$$H_y^{n+\frac{1}{2}}\left(i+\frac{1}{2}, j\right) = H_y^{n-\frac{1}{2}}\left(i+\frac{1}{2}, j\right) + \frac{\frac{k_y(m)}{\Delta t} + \frac{\sigma_y(m)}{2\varepsilon_0}}{\mu_1/\Delta t} \cdot B_y^{n+\frac{1}{2}}\left(i+\frac{1}{2}, j\right) - \frac{\frac{k_y(m)}{\Delta t} - \frac{\sigma_y(m)}{2\varepsilon_0}}{\mu_1/\Delta t} \cdot B_y^{n-\frac{1}{2}}\left(i+\frac{1}{2}, j\right) \tag{14}$$

$$P_z'^{n+1}(i, j) = \frac{\varepsilon_1(m)/\Delta t - 0.5\cdot\sigma_1(m)}{\varepsilon_1(m)/\Delta t + 0.5\cdot\sigma_1(m)} \cdot P'^n_z(i, j) + \frac{1}{\varepsilon_1(m)/\Delta t + 0.5\cdot\sigma_1(m)} \cdot \left[\frac{1}{\Delta x} \cdot \left(H_y^{n+\frac{1}{2}}\left(i+\frac{1}{2}, j\right) - H_y^{n+\frac{1}{2}}\left(i-\frac{1}{2}, j\right)\right) - \frac{1}{\Delta y} \cdot \left(H_x^{n+\frac{1}{2}}\left(i, j+\frac{1}{2}\right) - H_x^{n+\frac{1}{2}}\left(i, j-\frac{1}{2}\right)\right)\right] \tag{15}$$

$$P_z^{n+1}(i,j) = \frac{k_x(m)/\Delta t - \sigma_x(m)/(2\varepsilon_0)}{k_x(m)/\Delta t + \sigma_x(m)/(2\varepsilon_0)} P_z^n(i,j) + \frac{1/\Delta t}{k_x(m)/\Delta t + \sigma_x(m)/(2\varepsilon_0)} \left[{P'_z}^{n+1}(i,j) - {P'_z}^{n}(i,j) \right] \quad (16)$$

$$E_z^{n+1}(i,j) = \frac{k_y(m)/\Delta t - \sigma_y(m)/(2\varepsilon_0)}{k_y(m)/\Delta t + \sigma_y(m)/(2\varepsilon_0)} E_z^n(i,j) + \frac{1/\Delta t}{k_y(m)/\Delta t + \sigma_y(m)/(2\varepsilon_0)} \left(P_z^{n+1}(i,j) - P_z^n(i,j) \right) \quad (17)$$

where the subscript i and j are the grid point along x and y direction, and the subscript n is the number of time step. m is denoted as $(i, j+1/2)$ in Equations (11)–(12), $(i+1/2, j)$ in Equations (13)–(14), and (i, j) in Equations (15)–(17), respectively. Δx, Δy are the spatial increments in the x- and y-directions, and Δt is the time increment. To ensure the stability and accuracy of FDTD algorithm [18], in this paper, the spatial increment and temporal increment could be set as $\Delta x = \Delta y = \delta$, $\Delta t = 0.5 \times \delta / c$, and c is the light speed in vacuum. The finite- difference equations for the TE waves can be obtained by dual transformations, which are not presented here.

2.3. Connective Boundary

The connective boundary can divide the computation region into the total field region and the scattered field region. The total field region contains the incident field and the scattered field, but the scattered field region only includes the scattered field [19]. Next, it will be introduced how the incident wave is generated on the connective boundary.

In Fig. 3, a plane wave of unit amplitude $\overline{E_i} = \hat{z} \exp(j_0(\overline{k} \cdot \overline{r} + wt))$ $(j_0 = \sqrt{-1})$ propagates in the direction of θ_i relative to y-axis, and θ_i represents the incident angle. Let the propagation direction $\overline{k}$ as y'-axis, the direction $\overline{E_i}$ as z'-axis, and build the rectangular coordinate $x'y'z'$. The incident wave is computed using the 1-D FDTD method with the same spatial and temporal steps as the 2-D FDTD method mentioned above. The incident electric field of a series of points on y'-axis can be denoted as $E_i^n(p)$, and p is an integer. Thus, the projection of any point (i, j) on the connective boundary onto y'-axis is written as

$$y1 = i\Delta x \sin\theta_i - j\Delta y \cos\theta_i \quad (18)$$

However, it is possible that $y1$ is not an integer and can not correspond to the node on the y'-axis. Let $p = floor(y1)$, $w1 = y1 - p$, where

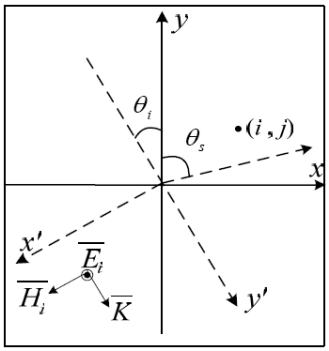

Figure 3. Projection model of the node on the connective boundary onto the y'-axis.

p represents the maximum integer less than $y1$. The incident electric field of any point (i, j) is obtained by linear interpolation

$$E'_z = (1 - w1)\, E_i^n\,(p) + w1 E_i^n\,(p+1) \tag{19}$$

Similar to the derivation of (19), the incident magnetic field is expressed as

$$H'_x = (1 - w1)\, H_i^n\,(p) + w1 H_i^n\,(p+1) \tag{20}$$

Thus, in the reference coordinate xyz

$$\begin{cases} E_{z,i}\,(i,j) = E'_z \\ H_{x,i}\,(i,j+1/2) = -H'_x \cos\theta_i \end{cases} \tag{21}$$

After introducing the incident wave, the finite-difference equations on the connective boundary should be updated as [19]

$$\begin{aligned} E_z^{n+1}\,(i,j) \;=\; & E_z^n\,(i,j) + \frac{\Delta t}{\varepsilon}\left[\nabla \times \overline{H}\right]_z^{n+1/2} \\ & - \frac{\Delta t}{\varepsilon}\frac{H_{x,i}^{n+1/2}\left(i, j+\frac{1}{2}\right)}{\Delta y} \end{aligned} \tag{22}$$

$$\begin{aligned} H_x^{n+1/2}\left(i, j+\frac{1}{2}\right) \;=\; & H_x^{n-1/2}\left(i, j+\frac{1}{2}\right) \\ & - \frac{\Delta t}{\mu}\left[\nabla \times \overline{E}\right]_x^n - \frac{\Delta t}{\mu}\cdot\frac{E_{z,i}^n\,(i,j)}{\Delta y} \end{aligned} \tag{23}$$

In numerical simulations of composite scattering, finite-length rough surface must be used to model scattering from infinite surface.

When a plane wave strikes the finite-length rough surfaces, boundary reflection occurs. One way of minimizing reflection is to construct an incident wave that tapers to very small values at the surface edges. Reflection still occurs, but it makes negligible contributions to the scattered field. To solve this problem, Fung et al. [20] put forward the Gaussian window function to guard against the truncation effect. And the Gaussian window function is expressed as

$$G(x,y) = \exp\left\{-\left[(x-x_0)^2 + (y-y_0)^2\right]\left(\frac{\cos\theta_i}{T}\right)^2\right\} \tag{24}$$

where x_0 and y_0 are the spatial coordinates at the center of the connective boundary. T is a constant which determines the width of the window function, $\cos\theta_i/T = 2.6/\rho_m$ and ρ_m is the minimum distance from the center (x_0, y_0) to the surface edge.

2.4. Output Boundary

The near fields for the composite model of target and underlying two-layered rough surfaces can be obtained on the basis of theory described above. As indicated in [19], a way to obtain the far fields is to do a near-to-far field transformation, which is based on the surface equivalence theorem. The transform formula for the output boundary is expressed as

$$\overline{E_s} = \hat{z}\frac{1}{2}\sqrt{\frac{j_0 k}{2\pi r}}\exp\left(-j_0 kr\right)\left(-zf_z - f_{mx}\sin\phi\right) \tag{25}$$

where, $j_0 = \sqrt{-1}$ and k is the incident wave number, $k = |\overline{k}|$. r is the distance from the origin in the reference coordinate to any point at infinity and $z = \sqrt{\mu_0/\varepsilon_0}$ is the impedance. ϕ represents the angle between the direction of scattered field and x-axis, where $\phi = 90^\circ - \theta_s$, θ_s is scattered angle (shown in Fig. 3). f_z and f_{mx} are the terms which are related to the equivalent surface electric and magnetic currents [19]. The radar scattering coefficient in the far zone is defined as [21]

$$\sigma = \lim_{r\to\infty}\frac{2\pi r}{L}\frac{\left|\overline{E_s}\right|^2}{\left|\overline{E_i}\right|^2} \tag{26}$$

3. NUMERICAL RESULTS AND DISCUSSIONS

In this section, for the composite electromagnetic scattering of cylinder located above two-layered rough surfaces as an example, the

angular distribution of scattering coefficient for different conditions are computed and analyzed in detail. For convenience, some parameters describing the cylinder and two-layered rough surfaces are measured in wave length λ. And the length of rough surfaces $L = 180\lambda$, the spatial increment is taken as $\Delta x = \Delta y = \delta = \lambda/20$, the UPML thickness is 5δ. The numerical results presented in the following are the average of 45 Monte Carlo realizations.

In order to ensure the validity of FDTD algorithm presented in the paper, in Fig. 4, we firstly compute the angular distribution of bistatic scattering coefficient from a PEC cylinder with radius λ and altitude of $h = 2\lambda$ above a single-layered PEC Gaussian rough surface using the conventional MOM and FDTD, respectively. Where the parameters related to rough surface is $\sigma = 0.2\lambda$, $l = 1.5\lambda$, and the TM-polarized incidence wave with frequency 0.3 GHz is considered. The results from the conventional MOM are obtained in [22]. It is obvious that the angular distribution of scattering coefficient for both incident angle 30° [Fig. 4(a)] and incident angle 60° [Fig. 4(b)] by FDTD is in good agreement with that obtained by MOM except for the grazing scattering angles, which demonstrates the feasibility and applicability of FDTD algorithm.

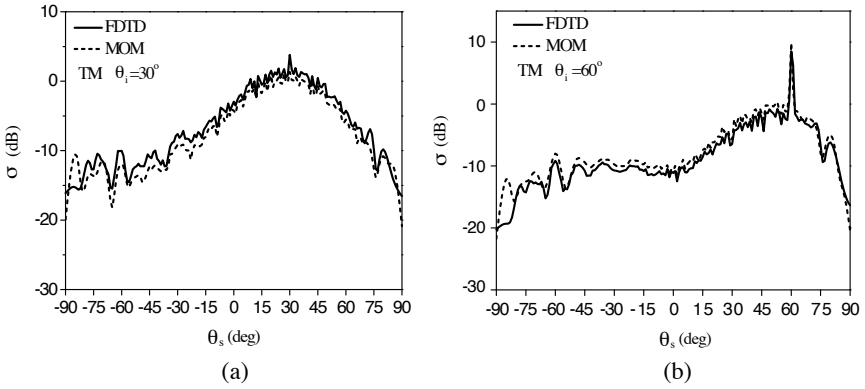

Figure 4. Comparison of the two different methods for the bistatic scattering from a PEC cylinder above the single-layered PEC rough surface (a) $\theta_i = 30°$, (b) $\theta_i = 60°$.

In Fig. 5, the angular distribution of bistatic scattering coefficient from the PEC and dielectric cylinder ($r = 1.0\lambda$; $h = 2.0\lambda$; $\varepsilon_2 = 4 - 3j_0$) above two-layered surfaces ($\sigma_1 = 0.2\lambda$, $l_1 = 1.5\lambda$; $\sigma_2 = 0.1\lambda$, $l_2 = 1.4\lambda$; $H = 2.0\lambda$; $\varepsilon_3 = 2.5 - j_0 0.18$, $\varepsilon_4 = 9.8 - j_0 1.2$) is investigated for TE polarization [Fig. 5(a)] and TM polarization [Fig. 5(b)]. Where the incident angle is $\theta_i = 30°$, and the incident frequency 1 GHz. It is clear

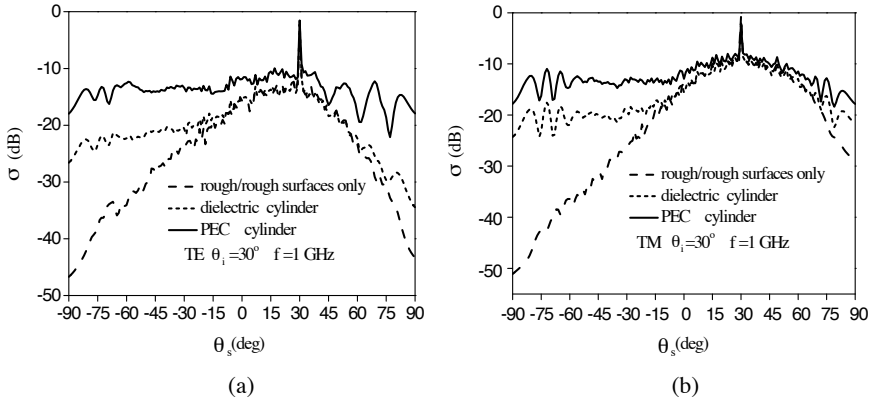

Figure 5. The bistatic scattering coefficient from the PEC/dielectric cylinder above two-layered rough surfaces (a) TE (b) TM.

that the angular pattern of composite scattering seems to be governed by two-layered rough surface scattering for different polarizations, this phenomenon is mainly caused by the fact that the object size is much smaller than that of the rough surface. It is also found that the scattering from composite model is much stronger than that of two-layered rough surfaces only far from the specular direction. In addition, we observed easily that the bistatic scattering from the PEC cylinder situated above rough surfaces is greater that that of dielectric cylinder above rough surfaces in all scattering direction, which results from the stronger reflection of PEC cylinder without absorption.

To further explore the important scattering characteristics of the cylinder-rough surface model, Fig. 6 shows the influence of dielectric constant ε_4 of the lower medium layer on the bistatic scattering coefficient when the dielectric parameter ε_3 of upper layer is a constant equal to 2.5. Fig. 6(a) indicates the result of two-layered rough surfaces only ($\sigma_1 = 0.2\lambda$, $l_1 = 1.5\lambda$; $\sigma_2 = 0.1\lambda$, $l_2 = 1.4\lambda$; $H = 2.0\lambda$), and Fig. 6(b) is the result with PEC cylinder ($r = 1.0\lambda$; $h = 2.0\lambda$) located above two-layered rough surfaces. The value of ε_4 in Fig. 6 is set as 0.5, 1.5, 2.5, 9.8, respectively, and when ε_4 is 2.5, the two-layered rough surfaces can be considered as a single-layered rough surface with infinite depth. As for the bistatic scattering of rough surfaces only in Fig. 6(a) is concerned, it can be seen that the bistatic scattering coefficient when $|\varepsilon_3 - \varepsilon_4|$ is small is approach to that of single-layered rough surface over the whole scattered angular range. Similar result can be obtained for the scattering of composite model of PEC cylinder and underlying rough surfaces under the small and moderate scattered

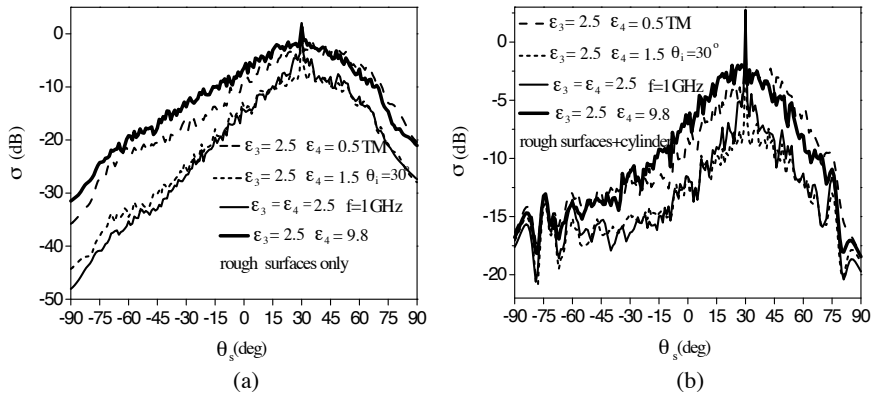

Figure 6. The bistatic scattering from lossless two-layered rough surfaces for different ε_4 (a) rough surfaces only (b) rough surfaces with PEC cylinder.

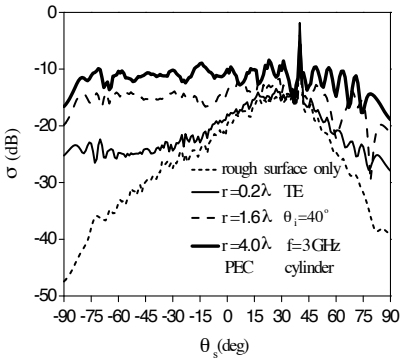

Figure 7. The composite scattering for different radius of cylinder r.

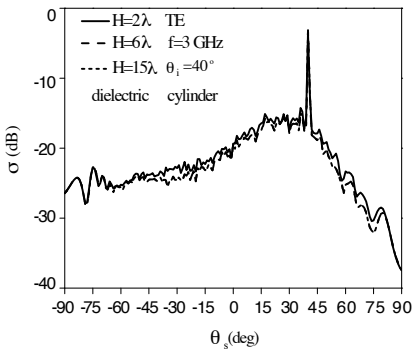

Figure 8. The composite scattering for different thickness H of upper medium.

angles.

In Fig. 7, the influence of the radius of cylinder r on the bistatic scattering coefficient of the PEC cylinder with the altitude of $h = 5\lambda$ above two-layered rough surfaces ($\sigma_1 = 0.2\lambda$, $l_1 = 1.5\lambda$; $\sigma_2 = 0.1\lambda$, $l_2 = 1.4\lambda$; $H = 2.0\lambda$; $\varepsilon_3 = 2.5 - j_0 0.18$, $\varepsilon_4 = 9.8 - j_0 1.2$) with TE polarization is also examined. In performing the calculation, the incident frequency is 3 GHz. It is clear that the bistatic scattering coefficient of composite model increases with increasing r far from the specular direction, especially in the large scattering direction. This

result is mainly due to the fact that the coupled scattering increases when the coupled area between cylinder and surface becomes greater with the increase of r, which results in the total bistatic scattering of composite model increases. That is to say, the power scattered by the cylinder increases with increasing the size of the PEC cylinder, and so does the scattering coefficient. In Fig. 8, the dependence of composite scattering from the cylinder ($r = 1.0\lambda$; $h = 2.0\lambda$; $\varepsilon_2 = 4 - 3j_0$) and two-layered rough surfaces on the thickness H of upper medium is presented. The parameters of rough surfaces are the same as the those in Fig. 7 except for H, and the thickness H is 2λ, 6λ, 15λ, respectively. It can be observed easily that the changes of the angular distribution of the composite scattering coefficient are "not sensitive" to the thickness of upper medium layered. In addition, we also investigated the effect of the altitude of cylinder h on the composite scattering and found that it is not obvious that the changes of the angular distribution of composite scattering coefficient versus h.

4. CONCLUSIONS

This paper presents a study of electromagnetic scattering from the target above the two-layered rough surfaces by using FDTD algorithm. The basic theory of FDTD method for calculating the scattered field is developed, including the generation of incident wave, the absorbing boundary conditions, and a transform from near- to far-field on the output boundary. And the numerical results of bistatic scattering from the PEC/dielectric cylinder above two-layered rough surfaces for different conditions are provided. Future investigation will include the electromagnetic scattering from the 3-D arbitrary target above 2-D single-layered rough surface and multilayered rough surfaces, and electromagnetic scattering from a number of targets above the rough surface with considering the multiple scattering of the targets.

ACKNOWLEDGMENT

This work was supported by the National Natural Science Foundation of China (Grant No. 60571058) and the Specialized Research Fund for the Doctoral Program of Higher Education, China (20070701010).

REFERENCES

1. Johnson, J. T., "A study of the four-path model for scattering from a target above a half space," *Microw. Opt. Techn. Lett.*, Vol. 30, No. 2, 130–134, 2001.

2. Kizilay, A. and S. Makal, "A neural network solution for identification and classification of cylindrical targets above perfectly conducting flat surfaces," *J. of Electromagn. Waves and Appl.*, Vol. 21, No. 14, 2147–2156, 2007.
3. Li, X. F., Y. J. Xie, and R. Yang, "High-frequency method analysis on scattering from homogenous dielectric objects with electrically large size in half space," *Progress In Electromagnetics Research B*, Vol. 1, 177–188, 2008.
4. Chen, X. J. and X. W. Shi, "Backscattering of electrically large perfect conducting targets modeled by NURBS surfaces in half-space," *Progress In Electromagnetics Research*, PIER 77, 215–224, 2007.
5. Zhang, Y., Y. E. Yang, H. Braunisch, and J. A. Kong, "Electromagnetic wave interaction of conducting object with rough surface by hybrid SPM/MOM technique," *Progress In Electromagnetics Research*, PIER 22, 315–335, 1999.
6. Wang, X., C. F. Wang, Y. B. Gan, and L. W. Li, "Electromagnetic scattering from a circular target above or below rough surface," *Progress In Electromagnetics Research*, PIER 40, 207–227, 2003.
7. Rodriguez, P. M., L. Landesa, J. L. Rodriguez, F. Obelleiro, and R. J. Burkholder, "The generalized forward-backward method for analyzing the scattering from targets on ocean-like rough surfaces," *IEEE Trans. Antennas Propag.*, Vol. 57, No. 6, 961–963, 1999.
8. Xu, L., Y. C. Guo, and X. W. Shi, "Dielectric half space model for the analysis of scattering from objects on ocean surface," *J. of Electromagn. Waves and Appl.*, Vol. 21, No. 15, 2287–2296, 2007.
9. Guo, L. X. and C. Y. Kim, "Light scattering models for a spherical particle above a slightly dielectric rough surface," *Microw. Opt. Techn. Lett.*, Vol. 33, No. 2, 142–146, 2002.
10. Li, J., L. X. Guo, and H. Zeng, "FDTD investigation on the electromagnetic scattering from a target above a randomly rough a sea surface," *Waves in Random and Complex Media*, Vol. 18, No. 4, 641–650, 2008.
11. Zhang, Y. and E. Bahar, "Mueller matrix elements that characterize scattering from coated random rough surfaces," *IEEE Trans. Antennas Propag.*, Vol. 57, No. 5, 949–955, 1999.
12. Fuks, I. M. and A. G. Voronovoch, "Wave diffraction by rough surfaces in an arbitrary plane layered medium," *Waves in Random Media*, Vol. 10, No. 2, 253–272, 2000.
13. Shenawee, M. E., "Polarimetric scattering from two-layered two-

dimensional random rough surfaces with and without buried objects," *IEEE Trans. Geosci. Remote Sensing*, Vol. 52, No. 1, 67–76, 2005.

14. Hu, B. and W. C. Chew, "Fast inhomogeneous plane wave algorithm for scattering from objects above the multilayered medium," *IEEE Trans. Geosci. Remote Sensing*, Vol. 39, No. 5, 1028–1038, 2001.
15. Kuga, Y. and P. Phu, "Experimental studies of millimeter wave scattering in discrete random media and from rough surfaces," *Progress In Electromagnetics Research*, PIER 14, 37–88, 1996.
16. Gedney, S. D., "An anisotropic perfectly matched layer-absorbing medium for the truncation of FDTD lattices," *IEEE Trans. Antennas Propag.*, Vol. 44, No. 12, 1630–1639, 1996.
17. Gedney, S. D., "An anisotropic PML absorbing media for the FDTD simulation for fields in lossy and dispersive media," *Electromagnetics*, Vol. 16, No. 4, 425–449, 1996.
18. Juntunen, J. S. and T. D. Tsiboukis, "Reduction of numerical dispersion in FDTD method through artificial anisotropy," *IEEE Trans. on Microwave Theory Tech.*, Vol. 58, No. 5, 582–588, 2000.
19. Taflove, A. and S. C. Hagness, *Computational Electrodynamics: The Finite-difference Time-domain Method*, Artech House, Boston, 1995.
20. Fung, A. K., M. R. Shah, and S. Tjuatja, "Numerical simulation of scattering from three-dimensional randomly rough surfaces," *IEEE Trans. Geosci. Remote Sensing*, Vol. 32, No. 5, 986–995, 1995.
21. Ruck, G., D. E. Barrick, W. D. Stuart, and C. K. Krichbaum, *Radar Cross Section Handbook*, Vol. 1, Plenum Press, New York, 1970.
22. Tsang, L., J. A. Kong, and K. H. Ding, *Scattering of Electromagnetic Waves*, Vol. 2, John Wiley & Sons, Inc., USA, 2001.